



# Oxidation resistance of aluminized refractory HfNbTaTiZr high entropy alloy



Ali Günen <sup>a,\*</sup>, Kadir Mert Döleker <sup>b</sup>, Erdogan Kanca <sup>c</sup>, Mst Alpona Akhtar <sup>d</sup>, Kunjal Patel <sup>d</sup>, Sundeep Mukherjee <sup>d</sup>

<sup>a</sup> Department of Metallurgy and Materials Engineering, Faculty of Engineering and Natural Sciences, Iskenderun Technical University, Hatay 31200, Turkey

<sup>b</sup> Department of Metallurgy and Materials Engineering, Faculty of Engineering, Ondokuz Mayıs University, Samsun 55139, Turkey

<sup>c</sup> Department of Mechanical Engineering, Faculty of Engineering and Natural Sciences, Iskenderun Technical University, Hatay 31200, Turkey

<sup>d</sup> Department of Materials Science and Engineering, University of North Texas, Denton, TX 76203, United States

## ARTICLE INFO

### Keywords:

Refractory high entropy alloys  
Aluminizing  
Characterization  
Oxidation resistance

## ABSTRACT

In the present study, an equimolar HfNbTaTiZr refractory high entropy alloy was subjected to powder-pack aluminizing at 950°C for 4 h. High-temperature isothermal oxidation tests were carried out in open air on both as-cast and aluminized samples at 1000°C for the durations of 5, 25, and 125 h. Microstructural analysis and oxidation kinetics revealed the formation of a complex oxide layer consisting of (Hf,Zr)O<sub>2</sub> and Al<sub>2</sub>O<sub>3</sub> with AlN inclusions in the aluminized samples following oxidation. Significant cracking of the complex oxide layer occurred after the prolonged exposure of 125 h. The as-cast samples followed similar oxidation kinetics under all the conditions. However, the magnitude of mass gain for the aluminized samples was 1.18, 1.55, and 3.60 times less than the as-cast samples after 5, 25, and 125 h of oxidation, respectively. The lower mass gain in the aluminized samples indicated the formation of an adherent oxide layer on the surface of the alloy and that the molar volume of the oxide equaled or exceeded the molar volume of the alloy. As a result, the aluminized alloy was shielded from direct contact with gaseous oxygen and oxidation rate was governed by diffusion through the oxide layer.

## 1. Introduction

Refractory metals have been long favored for ultra-high-temperature applications owing to their exceptionally high melting points [1]. The traditional definition of a refractory metal is an element with a melting point above 1800°C. Refractory metals have inherent limitations such as high density, low thermal expansion coefficient, high ductile-to-brittle transition temperature, and limited oxidation resistance [2–4]. To overcome these limitations and to achieve improved property combinations, alloying techniques have been employed [5]. In this context, refractory high entropy alloys (RHEAs) represent a new alloy design paradigm with multiple refractory constituent elements and the potential for use in extremely high temperatures, up to 1600°C [6]. The first RHEAs were based on the five refractory elements Mo, Nb, Ta, V, and W. Later, alloying elements from the first three rows of Group IV (Ti, Zr, Hf), Group V (V, Nb, Ta), and Group VI (Cr, Mo, and W) in the periodic table were included. More recently, low concentration (less than 5 %) of non-refractory metals such as Al, Co, Si, N, Ni, and Ti are also being

considered [7–9]. The main reason for the incorporation of these non-refractory alloying elements is to improve oxidation resistance, as most refractory metals tend to form porous, fast-growing, or volatile oxides at temperatures ranging from 600 to 800°C [6]. While fast-growing oxides can lead to the formation of a protective oxide scale, the generation of volatile oxides can lead to rapid deterioration, including flaking (spalling) and intergranular oxidation, with relatively complex mechanisms [5].

One of the primary limitations of current commercial refractory metals in high-temperature applications is their susceptibility to oxidation. Enhancing the oxidation resistance of RHEAs involves incorporating alloying elements such as Al, Cr, Si, and Ti, known for their role in forming protective oxides [10,11]. Chang et al. [12] investigated the oxidation behavior of TiZrNbHfTa RHEAs containing alloying additions of 0.3, 0.5, and 1.0 at% Al. Oxidation tests carried out at temperatures of 700, 900, 1100, and 1300°C for up to 100 h revealed increasing oxidation resistance with increasing Al content. The oxides that formed on the surface were complex, and oxidation resistance

\* Corresponding author.

E-mail address: [ali.gunen@iste.edu.tr](mailto:ali.gunen@iste.edu.tr) (A. Günen).

decreased rapidly with increasing temperature. The effect of 1 at% Si on the oxidation resistance of an AlNbMoCrTi RHEA was investigated at 900, 1000, and 1100°C by Gorr et al. [13]. Alloying with Si improved the oxidation resistance of the alloy, and analysis of the oxide layer formed revealed a complex composition rich in Cr and Al. Thermogravimetric measurements made at 1000°C and 1100°C revealed parabolic oxidation kinetics which transitioned to linear with prolonged exposure. Liu et al. [14] explored the effects of alloying elements, such as Cr, Al, and Si, on the oxidation resistance of four different RHEAs: NbCrMoTiAl<sub>0.5</sub>, NbCrMoVAl<sub>0.5</sub>, NbCrMoTiVAl<sub>0.5</sub>, and NbCrMoTiVAl<sub>0.5</sub>Si<sub>0.3</sub>. At 1300°C, the oxidation kinetics of all the RHEAs were linear. The resistance to oxidation was significantly improved with the addition of Ti and Si but worsened with the addition of V. In a study on the effects of Al and Al-Mo alloying additions (TiNbTa<sub>0.5</sub>ZrAl and TiNbTa<sub>0.5</sub>ZrAlMo<sub>0.5</sub>) on the high-temperature oxidation behavior of a TiNbTa<sub>0.5</sub>Zr RHEAs, Cao et al. [15] found that the oxidation rates of TiNbTa<sub>0.5</sub>Zr and TiNbTa<sub>0.5</sub>ZrAl were diffusion-controlled and followed an exponential relationship, whereas the oxidation rate of TiNbTa<sub>0.5</sub>ZrAlMo<sub>0.5</sub> was controlled by the interfacial reaction and showed a linear dependence. The authors reported that while the addition of Al improved the oxidation resistance by forming a protective oxide barrier, the addition of Mo with Al caused a significant decrease in oxidation resistance by creating large pores and cracks within the oxide layer.

Although the addition of oxide-forming elements such as Al, Cr, and Si seems to enhance oxidation resistance at high temperatures, there is a trade-off. The formation of brittle intermetallic compounds such as MoSi<sub>2</sub>, Nb<sub>3</sub>Al, and NbCr<sub>2</sub> may occur, impairing the ductility and toughness of the alloy [16]. Given the challenges associated with alloying for increased oxidation resistance in ductile RHEAs, surface coating and modification emerge as attractive alternatives [17,18], where elements that tend to form passivating oxides, such as Al, Cr, or Si, can be incorporated into the alloy, so that more protective oxide scales such as Al<sub>2</sub>O<sub>3</sub>, Cr<sub>2</sub>O<sub>3</sub>, and SiO<sub>2</sub> are formed during oxidation. A particularly promising technology in this regard is aluminizing which creates aluminum-rich coatings to increase oxidation resistance [19]. Sheikh et al. [20] conducted a study in which they subjected ductile RHEAs Hf<sub>0.5</sub>Nb<sub>0.5</sub>Ta<sub>0.5</sub>Ti<sub>1.5</sub>Zr and Al<sub>0.5</sub>Cr<sub>0.25</sub>Nb<sub>0.5</sub>Ta<sub>0.5</sub>Ti<sub>1.5</sub> to aluminizing treatments using three different aluminizing powder pack mixtures to improve their oxidation resistance. The authors reported that pest oxidation, a form of catastrophic accelerated oxidation, could be significantly reduced with the correct choice of aluminizing powder pack mixture. However, they noted that several issues remain to be resolved in the aluminizing of RHEAs. Powder-pack siliconizing of NbMoTaWV was successfully carried out Yi et al. [21] at siliconizing temperatures of 1100, 1200, and 1300°C. A single-phase (NbMoTaWV)Si<sub>2</sub> layer was generated on the surface at 1100 °C, while a double-layered coating consisting of a (NbMoTaWV)Si<sub>2</sub> layer and a mixed (NbMoTaWV)Si<sub>2</sub>/(NbMoTaWV)<sub>5</sub>Si<sub>3</sub> interdiffusion layer was obtained at 1200 and 1300°C. Coating thickness and the presence of cracks were influenced by process parameters, affecting the oxidation resistance. Oxidation tests of the coated samples performed at 1200°C for 96 h revealed corner distortion in most of the coatings after 48 h. Nevertheless, the high entropy of the (NbMoTaWV)Si<sub>2</sub> alloy suppressed the rapid growth of oxides, and the formation of a thin and compact SiO<sub>2</sub> layer greatly improved the oxidation resistance. Similar results were reported by Kuang et al. [22]. Yang et al. [23] subjected a MoNbTaVW alloy to a combined pack siliconizing/aluminizing (Si/Al) treatment (carried out at 1000°C for 24 h) and investigated its short-term (20-min) oxidation response at 1350°C. The authors reported that the Si/Al pack cementation coating formed on the surface was approximately 80 µm thick and comprised several distinct layers, including a Si-rich (silicide) layer, an interdiffusion layer, an aluminide layer and an Al diffusion layer. After short-term oxidation, the weight of as-cast samples increased with the formation of composite oxides MoO<sub>3</sub>(g), WO<sub>3</sub>(g), Nb<sub>2</sub>O<sub>5</sub>(s), Ta<sub>2</sub>O<sub>5</sub>(s) and V<sub>2</sub>O<sub>5</sub>(s). In contrast, the pack siliconized/aluminized samples developed a protective composite coating consisting of

SiO<sub>2</sub> and Al<sub>2</sub>O<sub>3</sub>, effectively preventing excessive oxidation.

One important conclusion that can be derived from the studies mentioned above is that RHEAs tend to form complex oxide layers under oxidative environments, leading to intrinsically different oxidation behavior compared to conventional refractory alloys. The oxidation resistance varies depending upon the characteristics of the oxides and interlayer structures that are formed. For instance, in NbTiZrV and NbTiZrCr RHEAs it has been observed that NbCrO<sub>4</sub> tends to reduce oxidation [24]. In AlCrHfMoNbTiVW RHEAs, complex surface oxides like CrVNbO<sub>6</sub>, Nb<sub>9</sub>VO<sub>25</sub>, or TiNb<sub>2</sub>O<sub>7</sub> have limited effects [25]. Oxidation of Al<sub>0.5</sub>CrMoNbV, Al<sub>0.5</sub>CrMoNbTiV, Al<sub>0.5</sub>CrMoNbTiVSi<sub>0.3</sub>, and Al<sub>0.5</sub>Cr-MoNbTi results in complex surface oxides such as (TiCrNbV)O<sub>2</sub>, CrVNbO<sub>5</sub>, and NbCrO<sub>4</sub>, among which (TiCrNbV)O<sub>2</sub> provides the best oxidation resistance [14]. One general conclusion that could be reached regarding the oxidation of RHEAs is that alloying with Cr, Al, and Ti typically improves the oxidation resistance while V significantly reduces it [7,14,24].

In summary, RHEAs hold promise for high-temperature applications, but their oxidation resistance can be limiting. Among the RHEAs, HfNbTaTiZr, characterized by a BCC structure, is notable for its excellent high-temperature mechanical properties [26] and high resistance to surface degradation [27]. Additionally, this alloy holds promise for applications in solar [28] and nuclear energy [29]. The present study investigates the oxidation behavior of BCC HfNbTaTiZr RHEAs and explores aluminizing treatments to improve its high-temperature oxidation resistance.

## 2. Experimental procedure

### 2.1. Materials

High purity constituent elements (>99.9 %) were mixed in equiatomic proportions and arc-melted to synthesize the five-component HfNbTaTiZr RHEA. To ensure homogeneity and avoid elemental segregation, the alloy was subjected to five remelting cycles under an Ar atmosphere. Subsequently, it was cast into a water-cooled copper mold with dimensions of 60 mm × 10 mm × 5 mm. Inductively coupled plasma optical emission spectroscopy (ICP-OES) chemical analysis was conducted to determine the composition of the RHEA. The nominal composition of the alloy was found to be Hf<sub>20</sub>Nb<sub>20</sub>Ta<sub>20</sub>Ti<sub>20</sub>Zr<sub>20</sub> (at%), with standard deviation of less than ±0.2 at% for each of the constituent elements, as determined from 10 measurements at various locations.

### 2.2. Aluminizing

15 mm × 10 mm × 5 mm-sized samples were cut with wire electrical discharge machining (WEDM) from the 60 mm × 10 mm × 5 mm-sized samples for the aluminizing process. Following WEDM, the surfaces were ground using 1000-grit SiC abrasive papers to eliminate potential surface oxidation caused by WEDM. A powder-pack aluminizing medium consisting of 45 % Al (the aluminum source, 99.99 % purity, Alfa Aesar), 45 % Al<sub>2</sub>O<sub>3</sub> (the filler, Alfa Aesar), and 10 % NH<sub>4</sub>Cl (the activator, Alfa Aesar) powders underwent mechanical mixing for 1 h at 400 rpm to achieve a homogeneous powder mixture. The aluminizing treatment was carried out using hermetically sealed Inconel 718 containers. The samples were positioned such that at least 10 mm of aluminizing powder surrounded each sample on all sides, and about 20 mm of Al<sub>2</sub>O<sub>3</sub> powder was placed on top of the pack to prevent oxidation. The top of the container was tightly sealed with Inconel 718 fasteners before heating. The aluminizing process was carried out in a muffle furnace maintained at 950 °C for 4 h. At the end of the process, the container was immediately removed from the furnace, cooled in open air, and the samples were extracted as soon as the container temperature dropped below 50 °C. No additional cleaning of the coated surfaces was required as there was no observed adhesion of aluminizing powders to the sample surfaces.

### 2.3. Characterization and high-temperature oxidation tests

To examine the cross-sectional microstructures, the aluminized samples were cut to dimensions of 15 mm × 10 mm × 5 mm, and the cross-sections were subsequently cold mounted, ground using 320–2500 grit SiC papers, and polished using 0.25  $\mu\text{m}$   $\text{Al}_2\text{O}_3$  paste. No etching was applied. The cross-sectional microstructures of the aluminized  $\text{HfNbTaTiZr}$  RHEAs were characterized using a Thermo Fisher Scientific Apreo S scanning electron microscope (SEM) operating at 30 kV, equipped with a concentric backscatter detector (CBS). X-ray diffraction (XRD) analysis was performed using a computer-controlled Rigaku SmartLab DMAX 2200 diffractometer with  $\text{Cu K}$  radiation ( $\lambda = 0.154$  nm) and a 2 $\theta$  range of 10° to 90° to confirm the presence of aluminides and/or other phases formed on the surface as stated in previous studies [30,31].

The as-cast and aluminized  $\text{HfNbTaTiZr}$  RHEAs were subjected to isothermal oxidation testing at 1000 °C for 5, 25 and 125 h in an Protherm HLF 120/20 electric furnace (Turkey) in open air. Before and after each oxidation test, the samples were weighed using an analytical balance with an accuracy of  $1 \times 10^{-4}$  g. For the mean oxide thickness measurements, 10 measurements were taken from each SEM image (five for every experimental condition). XRD analyses were performed on the samples before and after oxidation using a Rigaku SmartLab DMAX 2200 diffractometer (Japan) within the 2 $\theta$  range of 10° to 90° to identify the phases. Then, cross-sections of the oxidized samples were cold mounted and polished and examined via SEM imaging and EDS. The growth rate constant ( $n$ ) was calculated from the oxide thickness and time data using the following equation:

$$\Delta m = Kt^n \quad (1)$$

The value of  $n$  for each alloy was determined from the slope of the plots of  $\Delta m/A$  versus  $t$ , where  $\Delta m$  and  $A$  represent the change in mass and surface area, respectively,  $t$  is the oxidation time, and  $K$  is a constant.

## 3. Results and discussion

### 3.1. Characterization before high temperature oxidation

XRD patterns of the as-cast and aluminized  $\text{HfNbTaTiZr}$  RHEAs are shown in Fig. 1. The diffraction patterns of the as-cast  $\text{HfNbTaTiZr}$  (Fig. 1a) reveal the presence of the expected BCC phase, along with minor signs of oxidation manifested as  $(\text{Hf},\text{Zr})\text{TiO}_4$ . The aluminized

$\text{HfNbTaTiZr}$  RHEA (Fig. 1b), on the other hand, primarily consists of  $\text{AlN}$  and  $\text{NbZrAl}_6$ . In a recent study on  $\text{HfNbTaTiZr}$  RHEAs, Sadeghilaridjani et al. [32] observed a single BCC structure in the as-cast alloy. However, they did not detect any oxides on the surface after casting, a discrepancy which may be attributed to polishing of the samples prior to XRD analysis or better atmospheric control in their experimental setup.

SEM image of the as-cast  $\text{HfNbTaTiZr}$  RHEA shown in Fig. 2a. As seen in Fig. 2a, there are regions with three different color concentrations. These regions can be named as grizzled (Pt1), gray (Pt2) and dark (Pt3). It can be seen from the Table presented in the Fig. 2b that in EDS point analysis, the Pt1 region is the interdendritic region and the elements forming RHEAs differ slightly compared to the other two regions (Pt2 and Pt3). The relatively lower concentrations of Ti in the interdendritic regions suggest a tendency for Ti to segregate toward these regions. On the other hand, the Pt2 region has the most homogeneous chemical composition and is very close to the chemical composition of the target RHEAs produced. Therefore, EDS point analyzes taken from these three regions with different color concentrations on the figure can be said that these three regions have very similar compositions and the concentrations of alloying elements are closely aligned at the targeted 20 % level.

A cross-sectional SEM image of the near-surface region of the  $\text{HfNbTaTiZr}$  RHEA after aluminizing is shown in Fig. 3 along with EDS spot/line analyses. The cross-sectional microstructure reveals the presence of a uniform complex layer, approximately 65  $\mu\text{m}$  in thickness, across the surface. EDS spot analyses conducted at different depths within the complex layer (Pt1-Pt4) reveal high concentrations of aluminum and nitrogen. Relatively high levels of oxygen were also detected, indicating that minor oxidation took place during the aluminizing process. Interestingly, no oxides were identified in the diffraction pattern of the aluminized sample in Fig. 1b. This discrepancy may be attributed to the oxygen solubility of the alloy. Gorr et al. [5] suggested that the high oxygen solubility of the alloy creates an extended oxygen diffusion zone, potentially resulting in the cracking and spalling of the surface oxide layers. Trapped air between particles in the powder-pack aluminizing medium may have played a role in the oxygen dissolution and oxide formation during the aluminizing process. During aluminizing, aluminum initially reacts with nitrogen to form  $\text{AlN}$  [33]:



$\text{AlN}$  then reacts with oxygen to form trace amounts of  $\text{Al}_2\text{O}_3$  as follows [34]:



However, it should be noted that the  $\text{Al}_2\text{O}_3$  formation could not be confirmed in the diffraction patterns, and oxygen dissolution is therefore more likely.

Beneath the aluminized layer, there is a gradual decrease in aluminum concentration in the EDS line scan beyond a depth of approximately 65  $\mu\text{m}$ . This indicates that the thin layer beneath the aluminized layer is probably the aluminum diffusion zone. EDS spot analysis of the region exhibiting bright contrast just below the diffusion zone (the spot marked as Pt5) reveals an aluminum concentration measuring below 1 at% Al. This region is identified as the core and is essentially unaffected by aluminum diffusion.

### 3.2. Oxidation of as-cast $\text{HfNbTaTiZr}$

Diffraction patterns of the as-cast  $\text{HfNbTaTiZr}$  RHEA samples after oxidation at 1000 °C for 5, 25 and 125 h are shown in Fig. 4a, b, and c respectively. Initially, the oxide layer is predominantly composed of  $(\text{Hf}, \text{Zr})\text{O}_2$  (Fig. 4a). As oxidation progresses, hafnium and zirconium are depleted, leading to the subsequent formation of  $\text{TiO}_2$  and  $\text{Nb}_2\text{O}_5$  as titanium and niobium react with oxygen (Fig. 4b and c).

Gibbs free energy of formation values for the oxides of Hf, Zr, Ti, Ta, and Nb are included in Table 1. The data suggest that at 1000 °C, the

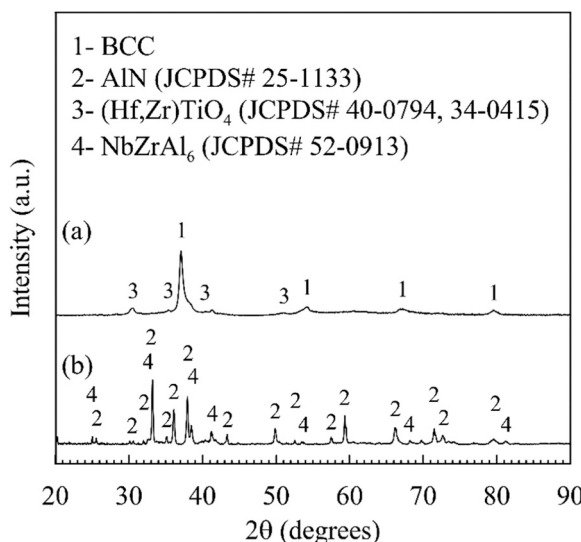


Fig. 1. Diffraction patterns obtained from the surface of the  $\text{HfNbTaTiZr}$  RHEA (a) as cast and (b) aluminized.

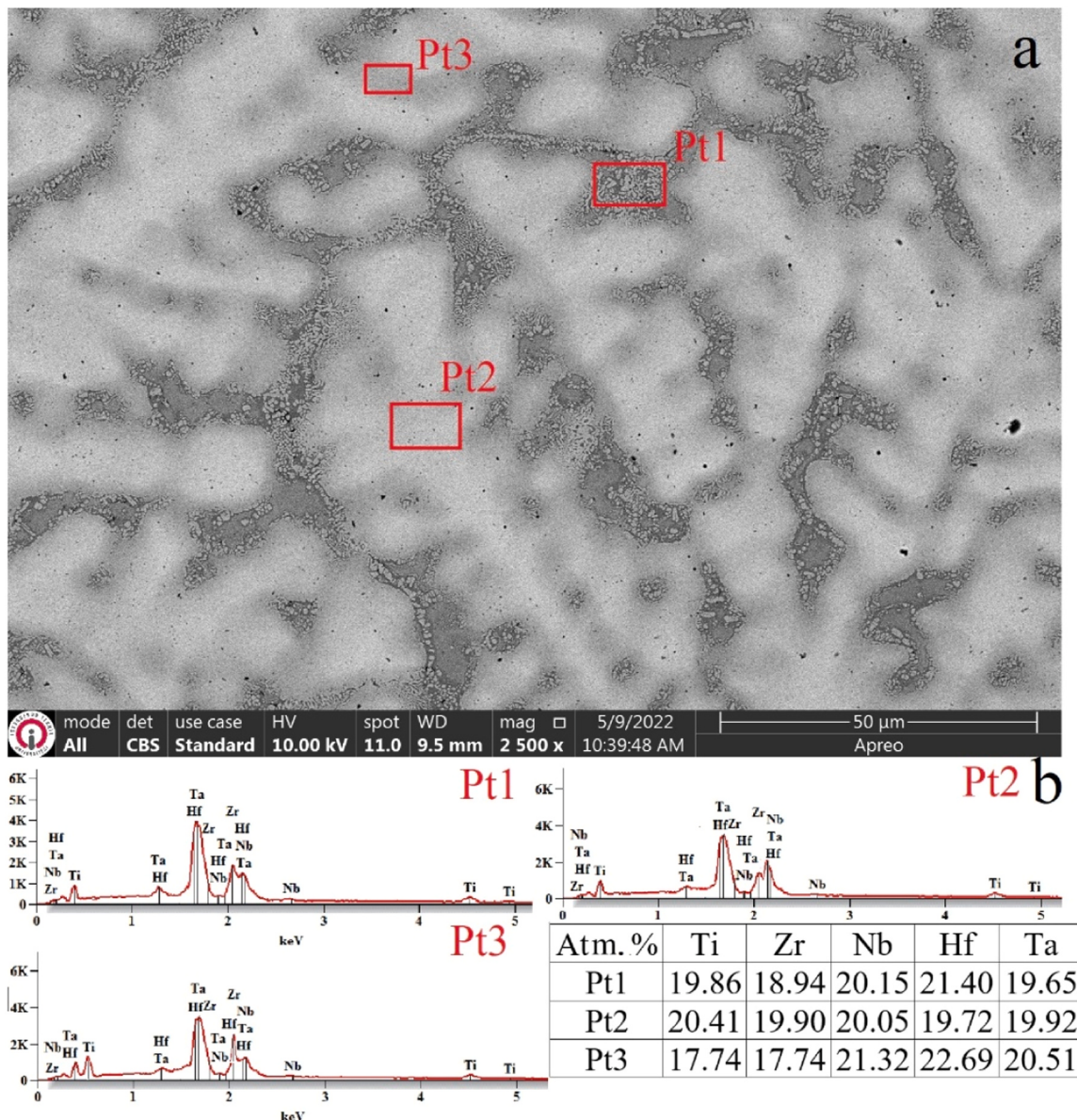


Fig. 2. Cross-sectional microstructure and EDS analysis as-cast HfNbTaTiZr RHEA (a) SEM image; (b) EDS spot analysis spectra.

three most thermodynamically stable oxides likely to form are HfO<sub>2</sub>, ZrO<sub>2</sub>, and TiO<sub>2</sub>. This is corroborated by the observed highest XRD peak intensities in Fig. 4(a, b) for HfO<sub>2</sub> and ZrO<sub>2</sub>, aligning with their respective Gibbs free energy values.

HfO<sub>2</sub> and ZrO<sub>2</sub> both featuring monoclinic crystal structures, combine to form a (Hf,Zr)O<sub>2</sub> solid solution. Comparatively, the peak intensities of Ta<sub>2</sub>O<sub>5</sub> and TiNb<sub>2</sub>O<sub>7</sub> increased significantly after 125 h of oxidation, as shown in Fig. 4(c). The presence of TiNb<sub>2</sub>O<sub>7</sub> (TiO<sub>2</sub>-Nb<sub>2</sub>O<sub>5</sub>) is attributed to the reaction between Nb and Ti with oxygen during high-temperature oxidation. This compound has also been observed in Nb-Ti alloy systems as well as other RHEAs [36,37]. It should be noted that due to the shallow depth of X-ray penetration, the body-centered cubic (BCC) phase in the substrate remained undetected in the oxidized RHEAs. The proposed reactions are as follows:



With increased oxidation time, (Hf,Zr)O<sub>2</sub> and Nb<sub>2</sub>O<sub>5</sub> react with TiO<sub>2</sub> to produce the orthorhombic (Hf,Zr)TiO<sub>4</sub> and TiNb<sub>2</sub>O<sub>7</sub> (TiO<sub>2</sub>-Nb<sub>2</sub>O<sub>5</sub>) phases as follows:



SEM images and of the as-cast HfNbTaTiZr RHEAs after oxidation for 5, 25 and 125 h are presented in Fig. 5 and the EDS spot analyses values for Fig. 5 are listed in Table 2.

Fig. 5a shows the formation of a ~200 μm thick oxide layer on the sample surface after a 5-h oxidation period. Cracking and flaking were observed in the topmost layer, where two EDS spot analyses were taken,

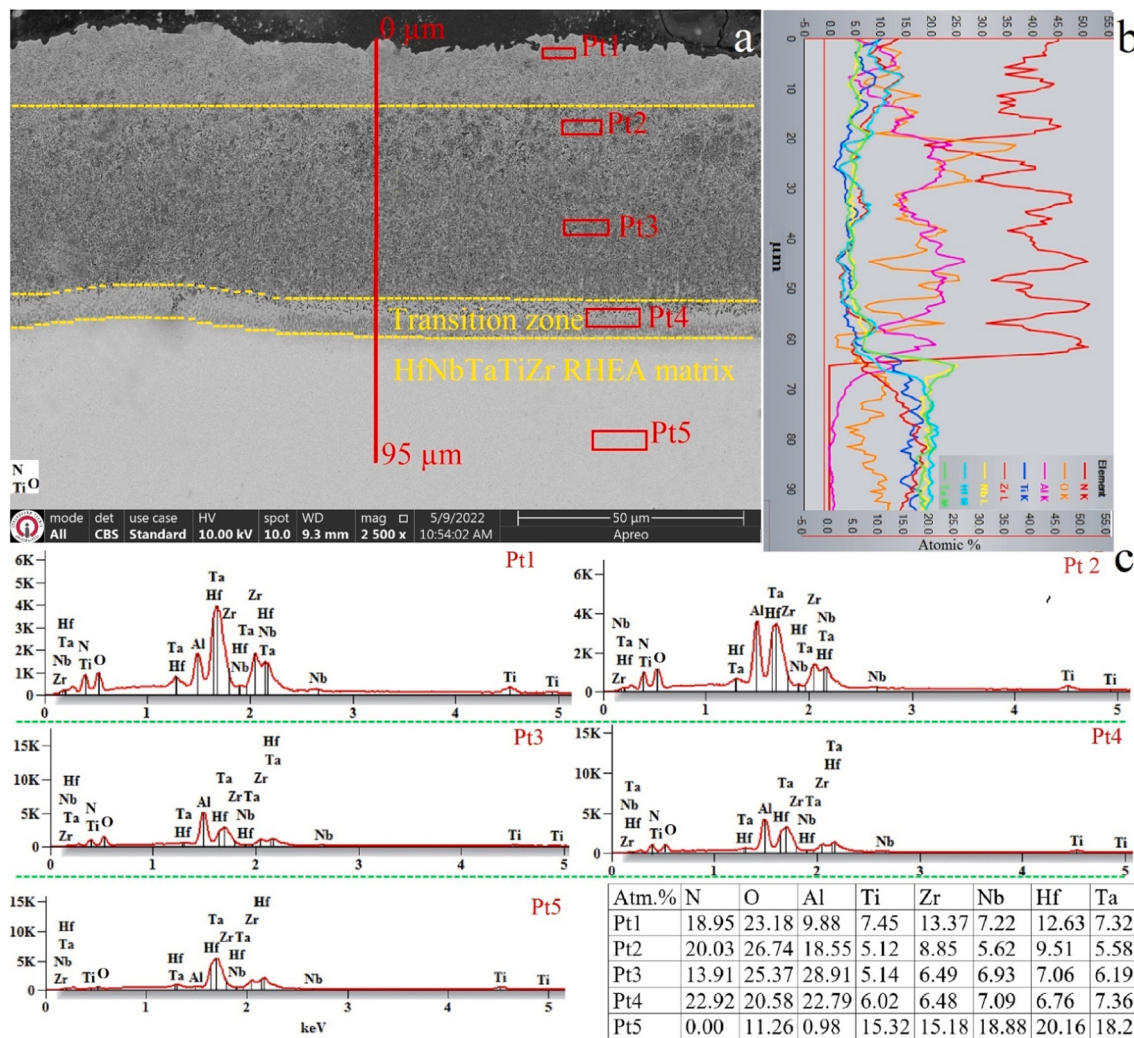


Fig. 3. Cross-sectional microstructure and EDS analysis results of the aluminized HfNbTaTiZr RHEA: (a) SEM image; (b) EDS line patterns; (c) EDS spot analysis spectra.

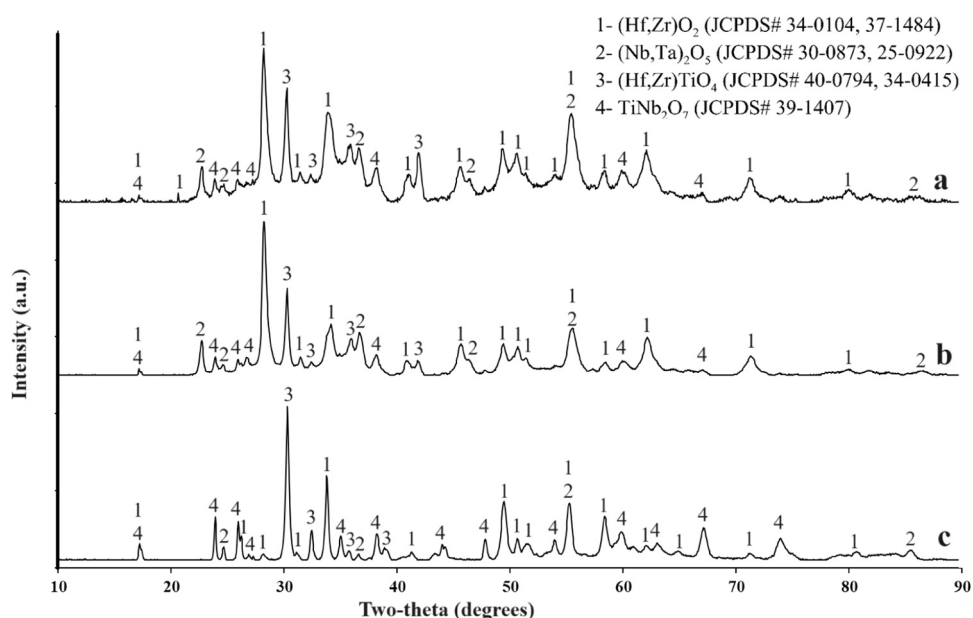
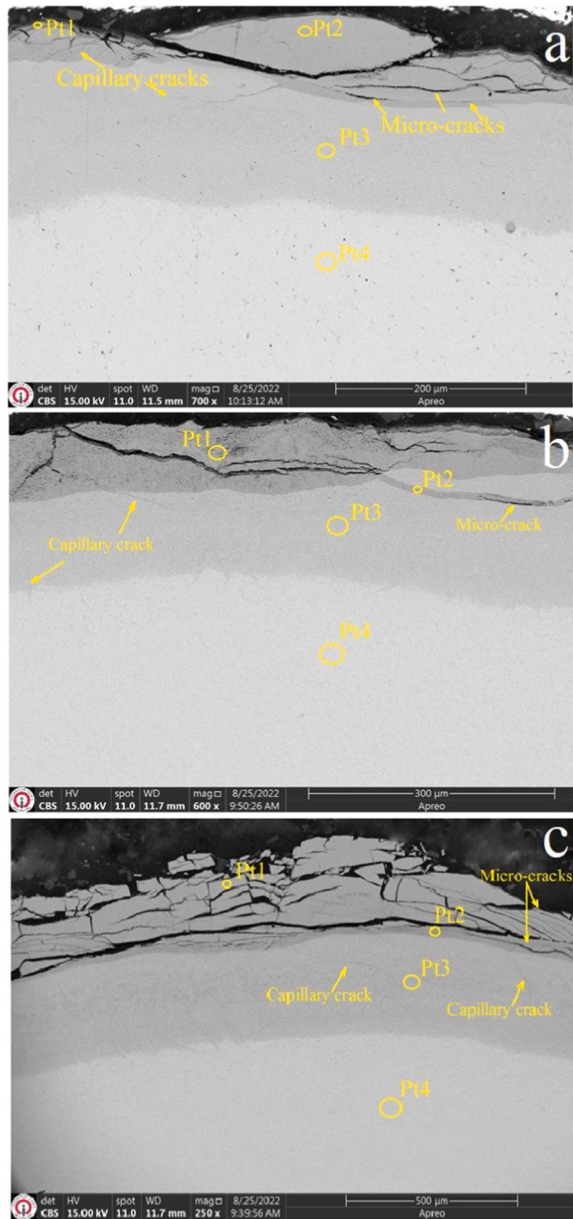


Fig. 4. Diffraction patterns obtained from the surface of the as-cast HfNbTaTiZr RHEA after oxidation at 1000°C for (a) 5, (b) 25, and (c) 125 h.

**Table 1**

Gibbs free energy of formation per mol O<sub>2</sub> of the oxides for hafnium, niobium, tantalum, titanium, and zirconium at 1000 °C [35].

Oxide	Nb <sub>2</sub> O <sub>5</sub>	Ta <sub>2</sub> O <sub>5</sub>	TiO <sub>2</sub>	ZrO <sub>2</sub>	HfO <sub>2</sub>
Gibbs Free Energy (kJ/mol)	-539.7	-596.9	-714.2	-858.9	-884.5



**Fig. 5.** SEM image of the as-cast HfNbTaTiZr RHEA after oxidation at 1000°C for (a) 5 h; (b) 25 h and (c) 125 h.

marked as Pt1 (dark contrast) and Pt2 (with bright contrast). Somewhat higher titanium and niobium concentrations in Pt1 suggest the presence of the (Hf,Zr)TiO<sub>4</sub> and TiNb<sub>2</sub>O<sub>7</sub> phases, with TiNb<sub>2</sub>O<sub>7</sub> concentrated at the surface. Beneath the topmost layer is a relatively crack-free layer with brighter contrast (Pt3). The relatively lower titanium content of this layer suggests the predominance of (Hf,Zr)O<sub>2</sub> and Nb<sub>2</sub>O<sub>5</sub> phases. Beneath this layer is the RHEA core with an even brighter contrast. EDS spot analysis of the core, marked as Pt4, revealed significantly lower oxygen content (refer to Table 2). However, the fact that the oxygen content did not drop to zero indicates interstitial diffusion of oxygen due

to the high temperature involved [12]. The extensive cracking of the topmost layer may be attributed to differences in the coefficient of thermal expansion (CTE) between the two layers, which may have been caused by volumetric or crystal structure differences [38]. Both (Hf,Zr)TiO<sub>4</sub> and TiNb<sub>2</sub>O<sub>7</sub> have been reported to be detrimental to high temperature oxidation resistance [39,40]. In titanium-aluminum alloys, rapid growth of TiO<sub>2</sub> may be suppressed by alloying with low concentration of niobium; a high niobium concentration, on the other hand, can lead to the formation of TiNb<sub>2</sub>O<sub>7</sub>, which reduces oxidation resistance. In this study, the formation of TiNb<sub>2</sub>O<sub>7</sub> in HfNbTaTiZr also appears to have had a similar effect on the oxidation resistance. Cracking due to TiNb<sub>2</sub>O<sub>7</sub> formation was previously observed in a study on an Al<sub>0.5</sub>Cr<sub>0.25</sub>Nb<sub>0.5</sub>-Ta<sub>0.5</sub>Ti<sub>1.5</sub> HEA [41], where EDS spot analyses and diffraction patterns suggested a complex distribution of oxides.

When the oxidation period was extended to 25 h (Fig. 5b), the oxide layer thickness increased to ~250 μm. Localized cracks observed in the topmost layer in the 5-h sample were replaced with more widespread, continuous cracks. EDS spot analysis of the topmost layer marked as Pt1 (Fig. 5b) again showed relatively higher Ti and Nb content compared to the underlying layer suggesting the presence of TiNb<sub>2</sub>O<sub>7</sub>. Capillary cracks and microcracks decreased in the underlying layers (Fig. 5b, spots marked as Pt2 and Pt3), and oxygen concentrations also dropped by more than 15 % in this layer (refer to Table 2), possibly due to the absence of TiNb<sub>2</sub>O<sub>7</sub>.

After 125 h of oxidation, the thickness of the oxide layer increased to ~500 μm (Fig. 5c) and substantial cracking was observed in the topmost layer, with oxygen concentrations reaching as high as 70 at%, according to EDS spot analysis (spots marked Pt1 and Pt2, also see Table 2). Extensive microcracking in HfO<sub>2</sub>-TiO<sub>2</sub> mixtures containing 30–40 % TiO<sub>2</sub> has been attributed to anisotropic thermal expansion [42]. An increase in the duration of oxidation therefore results in an increasing proportion of TiO<sub>2</sub> formation at high temperatures, leading to more complex oxides. It has been reported that the formation of metastable HfTiO<sub>4</sub> at high temperatures also tends to cause microcracking [43,44].

Therefore, considering the oxidation behavior of as-cast HfNbTaTiZr RHEA, it can be concluded that as the oxidation time was increased, more oxygen was allowed to diffuse into the alloy. The increased cracking in the outermost oxide layer enhanced the penetration of oxygen into the interior of the RHEA.

### 3.3. Oxidation of aluminized HfNbTaTiZr

Diffraction patterns of the aluminized HfNbTaTiZr RHEA samples after oxidation at 1000°C for 5, 25 and 125 h are shown in Fig. 6. Four different oxides, (Hf,Zr)O<sub>2</sub>, (Hf,Zr)TiO<sub>4</sub>, (Nb,Ta)<sub>2</sub>O<sub>5</sub>, and Al<sub>2</sub>O<sub>3</sub>, were detected in the oxidized sample. Al<sub>2</sub>O<sub>3</sub>, (Hf,Zr)O<sub>2</sub> and (Nb,Ta)<sub>2</sub>O<sub>5</sub> resulted from the reaction between the corresponding metals in HfNbTaTiZr and oxygen, while the complex oxides of (Hf,Zr)TiO<sub>4</sub> resulted from diffusion/reactions between HfO<sub>2</sub>, ZrO<sub>2</sub> and Nb<sub>2</sub>O<sub>5</sub> with TiO<sub>2</sub>. Despite the aluminizing treatment, aluminum-containing phases are not the dominant phase in the diffraction patterns of the samples. This can be attributed to the partial spalling of the aluminum-containing layers during the cooling stage in the oxidation process. In addition, BCC substrate diffraction patterns could not be detected due to the shallow depth of X-ray penetration.

SEM images and of the aluminized HfNbTaTiZr RHEAs after oxidation for 5, 25 and 125 h are presented in Fig. 7 and EDS spot analyses values are listed in Table 3.

Compared to the as-cast HfNbTaTiZr RHEA, which exhibited a ~65 μm thick oxide layer on its surface after 5 h of oxidation, the aluminized HfNbTaTiZr RHEA (Fig. 7a) showed a ~90 μm thick oxide layer. Three distinct regions were identified in the cross-sections of the aluminized samples after 5, 25, and 125 h of oxidation: (i) a porous oxide layer, (ii) a relatively pore-free oxide layer with darker contrast, and (iii) an aluminide/nitride layer with brighter contrast. All the layers displayed varying thickness. In contrast to the study by Sheikh et al.

**Table 2**  
EDS spot analysis values for Fig. 5.

Sample	Region	O-K	Ti-K	Zr-L	Nb-L	Hf-L	Ta-L
As-cast HfNbTaTiZr, oxidized for 5 h	Pt1	65.64	7.42	3.46	10.27	6.44	6.77
	Pt2	68.40	6.48	4.96	8.22	5.96	5.98
	Pt3	67.56	6.55	4.76	8.21	6.65	6.26
	Pt4	20.02	16.39	8.33	23.47	15.80	15.99
As-cast HfNbTaTiZr, oxidized for 25 h	Pt1	68.13	7.06	3.71	9.39	5.70	6.01
	Pt2	68.71	6.13	4.74	7.67	6.29	6.45
	Pt3	53.12	9.05	6.56	12.28	9.88	9.11
	Pt4	20.21	15.85	9.72	20.72	16.81	16.69
As-cast HfNbTaTiZr, oxidized for 125 h	Pt1	70.03	6.20	4.84	7.68	5.60	5.65
	Pt2	70.91	5.77	4.26	7.80	5.54	5.72
	Pt3	55.54	9.24	8.11	9.76	9.20	8.15
	Pt4	23.15	14.97	14.04	17.72	17.52	12.58

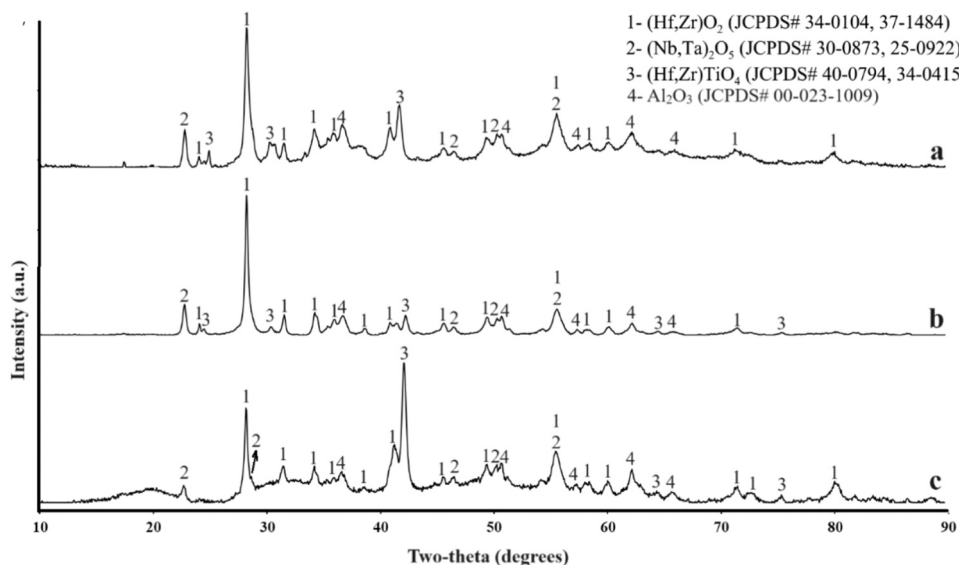


**Fig. 6.** Diffraction patterns obtained from the surface of the aluminized HfNbTaTiZr RHEA after oxidation at 1000°C for (a) 5, (b) 25, and (c) 125 h.

[11], the porous oxide and the underlying pore-free oxide layer in Fig. 7a shows very high concentrations of oxygen (77.52–67.71 at%, Table 3) and relatively high concentrations of aluminum (17.69–27.65 at%, Table 3) in the spots labelled Pt1 and Pt3, respectively. This suggests that aluminum oxides may have formed during the oxidation process, but the absence of aluminum-containing phases in Fig. 6 indicates that significant flaking occurred during the 5 h period. Immediately beneath these layers, the oxygen concentration drops to ~24 at% and the aluminum concentration increases to ~27 at% (Fig. 7a Pt4; Table 3), pointing to the presence of AlN and/or NbZrAl<sub>6</sub> phases in the underlying layer.

When the oxidation period was increased to 25 h, the oxide layer thickness increased to ~180 µm (Fig. 7b), nearly twice the thickness of the oxide layer observed compared to 5 h sample (Fig. 7a). Moreover, porosity and pitting were observed in the outermost part of the oxide layer. The increased oxidation duration also resulted in capillary cracks within the pore-free portion of the oxide layer, which may be due to the difference in coefficient of thermal expansion between the Al<sub>2</sub>O<sub>3</sub> layer and the core, as well as nitrogen evolution. However, these number of these cracks were significantly less compared to the oxidized as-cast samples. Accelerated oxidation may begin with oxygen infiltration through cracks, followed by oxygen diffusion into the substrate. EDS tests in Table 3 show higher O content in spots labelled as Pt1 and Pt2 of the 25 h sample (Fig. 7b) compared to the 5 h sample (Fig. 7a), while reduced oxygen and higher Al content were seen in the spots labelled as Pt3 and Pt4. This can be attributed to the porous oxidized zone, preventing oxygen from entering the interior.

When the oxidation time was increased to 125 h (Fig. 7c), the thickness of the oxide layer was expected to increase. However, as seen in Fig. 7c, the oxide layer on the surface is thinner compared to that of the 5 h and 25 h samples (Fig. 7a and Fig. 7b). The reason for this is the occurrence of pesting in the aluminide layer due to high temperature (1000 °C) and an extended oxidation period (125 h) (Fig. 7c). Indeed, Sheikh et al. [20], in their studies on the oxidation of aluminized Hf<sub>0.5</sub>Nb<sub>0.5</sub>Ta<sub>0.5</sub>Ti<sub>1.5</sub>Zr RHEAs, have reported that when a porous oxide layer forms in the aluminide layer, dependent on temperature and time, the increasing oxidation period does not prevent oxygen ingress through this porous oxide layer, resulting in the occurrence of pesting. In our study, similar to reference 20, as clearly seen in the region marked as Pt2 in Fig. 7b, the formation of porous structures is evident. Therefore, it is considered that in the 125 h sample, similar to the 25 h sample, this porous structure formed in the 25 h part of the oxidation test. During the continued process of the test (25–125 h), this porous structure, unable to prevent oxygen ingress, is evaluated as a cause of pesting, leading to a substantial delamination of the aluminide coating layer on the surface. The small portion of oxide layer that remained (the spot labelled as Pt1 in Fig. 7c) shows the presence of aluminum (9 at%; see Table 3) and a relatively high concentration of titanium (10 at%; see Table 3) indicating the formation of Al<sub>2</sub>O<sub>3</sub> and HfTiO<sub>4</sub> as discussed earlier. The two layers underneath this region in lighter contrast (Fig. 7c spots marked as Pt4) exhibit a high concentration of oxygen (~49 at% O and 0 at% Al; see Table 3). This indicates that the aluminum-rich layer was mostly lost by spalling after prolonged oxidation due to increase in oxygen concentration (20 at% at Pt5 in Fig. 7c) in the core.

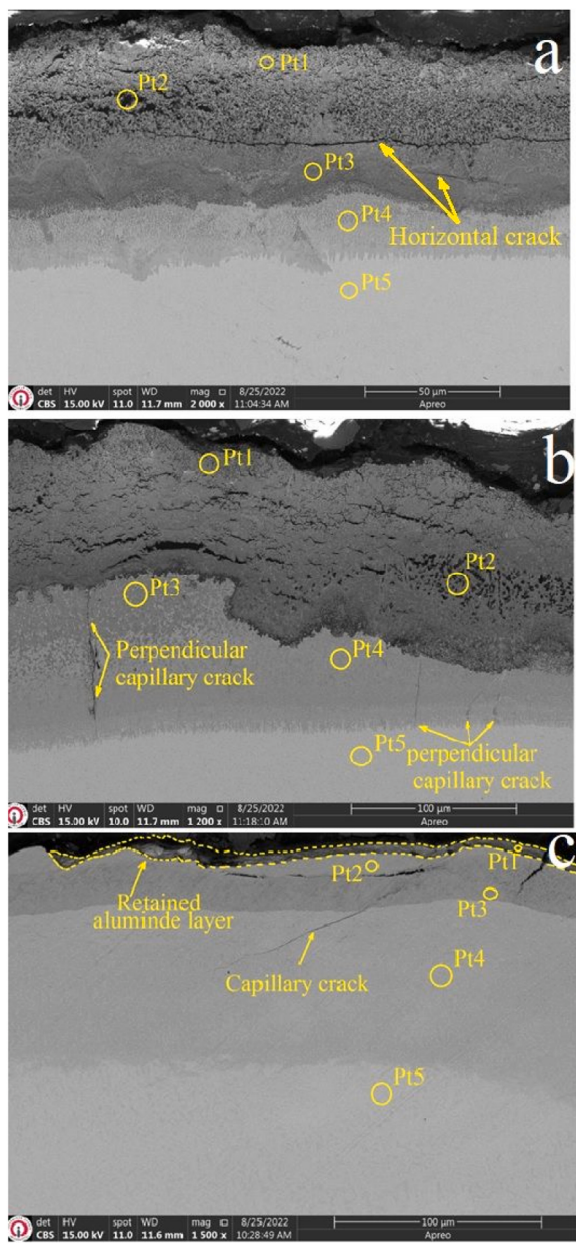


Fig. 7. SEM images of the aluminized HfNbTaTiZr RHEA after oxidation at 1000°C for (a) 5 h; (b) 25 h and (c) 125 h.

Table 3

EDS spot analysis values for Fig. 7.

Sample	Region	O-K	Al-K	Ti-K	Zr-L	Nb-L	Hf-L	Ta-L
Aluminized HfNbTaTiZr, oxidized for 5 h	Pt1	77.52	17.69	1.11	0.73	2.95	0.00	0.00
	Pt2	73.65	21.95	0.95	1.31	2.14	0.01	0.00
	Pt3	67.71	20.82	1.88	2.46	3.00	1.97	2.16
	Pt4	24.32	27.65	8.25	8.86	7.90	11.46	11.55
	Pt5	12.92	3.80	18.54	7.41	23.02	15.73	18.58
Aluminized HfNbTaTiZr, oxidized for 25 h	Pt1	76.33	18.74	0.98	0.79	3.15	0.00	0.01
	Pt2	68.22	21.76	1.41	1.79	3.47	1.16	2.18
	Pt3	33.40	48.31	3.40	3.50	3.98	3.75	3.65
	Pt4	2.81	51.48	8.94	7.60	8.15	10.99	10.02
	Pt5	16.17	1.32	16.66	12.41	18.62	17.25	17.57
Aluminized HfNbTaTiZr, oxidized for 125 h	Pt1	80.24	9.07	10.37	0.00	0.00	0.16	0.16
	Pt2	67.56	0.00	5.94	4.93	7.61	6.27	7.69
	Pt3	68.81	0.00	6.79	4.23	8.49	6.04	5.64
	Pt4	49.09	0.00	9.85	6.36	13.10	9.86	11.74
	Pt5	20.01	0.00	16.31	8.67	21.36	15.54	18.11

### 3.4. Kinetics of oxidation before and after aluminizing

The mass gain of the as-cast and aluminized HfNbTaTiZr RHEAs are plotted as a function of oxidation time in Fig. 8. Mass gain often occurs due to oxygen atoms diffusing into newly formed metals during high-temperature oxidation. The kinetic curve for 5 h oxidation both before and after aluminizing showed linear rate dependence, indicating solid state diffusion-controlled oxide scale growth. For 25 h oxidation, the alloy exhibited a two-stage kinetics, the initial oxidation rate was linear which then transitioned to a much slower growth. This implies that more unstable mixed oxide (metastable orthorhombic and spinel phases) formed first, followed by stable  $\text{Al}_2\text{O}_3$  phase formation as evidenced by increased percentage of Al (48–51 at%) in the intermediate Al rich zone (Fig. 7b Pt3/Pt4). It is believed that  $\text{Al}_2\text{O}_3$  layer increased the oxidation resistance of the alloy after 25 h, due to its slower oxygen transition (3 at % only, Fig. 7b Pt4) as compared to 5 h samples. This presents a moderately beneficial effect on the oxidation behavior of the RHEA for 25 h oxidation period in air at high temperatures. However, the alloy had rapid oxidation kinetics according to a linear growth rate law after 125 h of oxidation. When the surface oxide does not form a continuous protective oxide layer, linear oxide growth takes place. According to the linear oxidation kinetics, the high-temperature resistance-oxides are never dense or continuous structure and, can never separate oxygen into new metals.

The aluminizing process reduced the mass gain caused by oxidation for all the conditions studied here. This can be elucidated by the enduring stability exhibited by the AlN phase, which is generated on the surface coating at a temperature as high as 1638°C [45], alongside the exceptional resistance to high-temperature oxidation demonstrated by the  $\text{Al}_2\text{O}_3$  layer that evolves on the surface of the aluminide coating layer [30,46–48]. For the oxidation times of 5, 25, and 125 h,  $k_p$  rate constants of RHEA and the aluminized RHEA was found as 0.0027 g.  $\text{cm}^{-2}$  and 0.0101 g.  $\text{cm}^{-2}$ , respectively, supporting the superior oxidation resistance of the aluminized samples. This reduction in mass gain per unit surface area after aluminizing indicates that the volume of the surface oxide is equal to or greater than the volume of the alloy contributing to the reaction resulting in a well-adhered oxide [49]. The oxidation reaction rate is further controlled by the formation of a stable and crack-free oxide layer on the surface of the alloy which shields it from direct contact with gaseous oxygen and its diffusion through the oxide layer after aluminizing [20].

The aluminizing process reduced the mass gain caused by oxidation for all the conditions studied here. This can be elucidated by the enduring stability exhibited by the AlN phase, which is generated on the surface coating at a temperature as high as 1638°C [45], alongside the exceptional resistance to high-temperature oxidation demonstrated by the  $\text{Al}_2\text{O}_3$  layer that evolves on the surface of the aluminide coating layer [30,46–48]. For the oxidation times of 5, 25, and 125 h, the

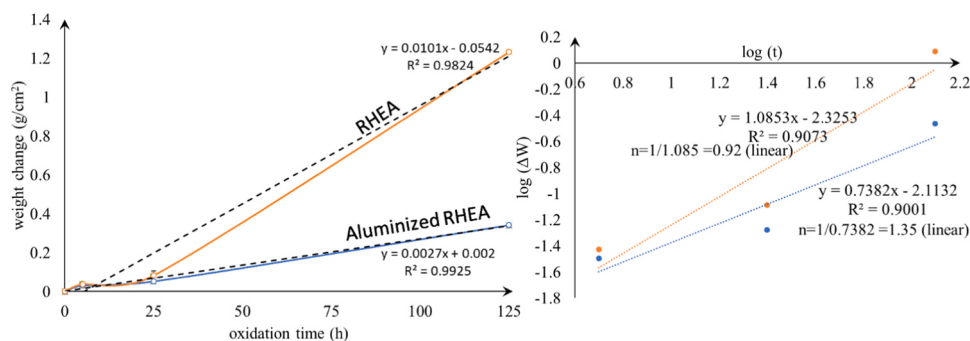


Fig. 8. Mass change per unit area versus oxidation time plot, and n value calculation plot.

aluminide coatings showed 1.18, 1.55, and 3.60 times less mass gain compared to the as-cast sample, respectively, supporting the superior oxidation resistance of the aluminized samples. This reduction in mass gain per unit surface area after aluminizing indicates that the volume of the surface oxide is equal to or greater than the volume of the alloy contributing to the reaction resulting in a well-adhered oxide [49]. The oxidation reaction rate is further controlled by the formation of a stable and crack-free oxide layer on the surface of the alloy which shields it from direct contact with gaseous oxygen and its diffusion through the oxide layer after aluminizing [20].

EDS analyses of regions underneath the oxide layer of the as-cast samples after 125 h of oxidation revealed relatively high oxygen concentrations, indicating that the oxide layers were not very effective in preventing oxygen penetration. In addition, mass of the alloy increased continuously despite fracture and spallation (Fig. 8). The linear shape of the oxidation curve and the fact that as oxidation duration increased, oxidation rate also did so provide support for this. The solubility of oxygen in the individual alloying elements in HfNbTaTiZr RHEA at 1000 °C is summarized in Table 4 [5]. The table shows especially high oxygen solubility for zirconium (30 %) and hafnium (20 %). Therefore, hafnium and zirconium likely impaired the oxidation resistance of the RHEA by (i) oxidizing rapidly to form non-protective oxides and (ii) dissolving significantly higher levels of interstitial oxygen, causing significant mismatch in thermal expansion between the oxide layer and the underlying RHEA eventually leading to flaking/spallation [50]. With the dissolution of oxygen in the alloy, the pesting oxidation trend caused the surface to shed in powder form after prolonged oxidation.

Considering the EDS results obtained from the sub-surface regions after the aluminizing process, it is observed that the oxygen amounts decreased. This shows that the oxide layers formed after the aluminizing process showed better protection and increased the oxidation resistance of the alloy. In aluminized specimens, alumina formed after oxidation deterred the penetration of oxygen. Sheikh et al. [20] reported improved oxidation resistance in aluminized  $Hf_{0.5}Nb_{0.5}Ta_{0.5}Ti_{1.5}Zr$  attributed to oxygen penetration through stress-induced surface cracks. Similar findings were observed in the present study, where after 25 h of oxidation, AlN resulted in perpendicular capillary cracks in the aluminized samples. Increased thermal stresses caused by the thermal expansion mismatch between the oxide layers, AlN and/or  $Nb_2ZrAl_6$  layers and the alloy at high temperature may have had a negative effect on the oxidation resistance. In another study [12], the effect on oxidation behavior was investigated by adding aluminum at different rates to the alloy ( $Al_xTi_xZr_xNb_xHf_xTa$ ) with the same content as our current study. It has been observed that increasing aluminum ratio improves the oxidation resistance of the alloy. However, the oxide layer formed, similar to

the present study, contained a high density of cracks. Oxygen solubility was similarly observed in the alloy despite the addition of aluminum. The formation of AlN (nitriding) is common in aluminized RHEAs and RHEAs alloyed with aluminum [41]. It is hypothesized that nitrogen evolution during the oxidation of AlN creates capillary cracks that damage the integrity of the oxide layer, promoting flaking and creating suitable pathways for oxygen transfer. Due to the flaking of the oxide layers with increased oxidation, no beneficial effect of the aluminizing process could be observed in the long-term oxidation tests.

#### 4. Conclusions

A powder-pack aluminizing process was used to significantly improve the oxidation resistance of a HfNbTaTiZr RHEA at 1000°C. For the as-cast RHEA, two oxide layers formed after oxidation for 125 h at 1000 °C: (i) a top layer with metastable oxides (such as  $(Hf,Zr)TiO_4$  and  $TiNb_2O_7$ ) and significant cracking and (ii) a bottom layer with stable oxides (such as  $HfO_2$ ,  $ZrO_2$ , and  $TiO_2$ ) and fine capillary cracks. In contrast, the aluminized RHEA showed a homogeneous and compact surface layer consisting primarily of  $Al_2O_3$ , AlN, and traces of  $Nb_2ZrAl_6$ . The thickness of the surface layers for the aluminized RHEA were 90  $\mu m$  and 180  $\mu m$  after 5 and 25 h of oxidation, respectively. This protective surface layer inhibited oxygen transport and enhanced oxidation resistance. However, after 125 h, the aluminide layer was depleted, causing significant pesting behavior marked by cracking, spalling-off, oxygen ingress, and accelerated oxygen dissolution at 1000°C. The aluminized RHEA showed 1.18, 1.55, and 3.60 times less weight gain compared to the as-cast RHEA after 5, 25, and 125 h of oxidation, respectively. Lower mass gain in aluminized samples suggests that the volume of surface oxide was equal to or greater than the alloy, protecting it from gaseous oxygen. While there is great potential for increasing the oxidation resistance of RHEAs through alloying, the aluminizing approach demonstrated here exhibits remarkable promise in advancing the use of RHEAs in ultrahigh temperature environments.

#### CRediT authorship contribution statement

**Kadir Mert Döleker:** Writing – review & editing, Writing – original draft, Methodology, Formal analysis, Data curation. **Erdogan Kanca:** Visualization, Validation, Investigation, Data curation. **Mst Alpona Akhtar:** Writing – review & editing, Writing – original draft, Methodology, Formal analysis. **Kunjal Patel:** Visualization, Software, Formal analysis, Conceptualization. **Sundeep Mukherjee:** Writing – review & editing, Writing – original draft, Validation, Supervision, Conceptualization. **Ali Gunen:** Writing – review & editing, Writing – original draft, Validation, Supervision, Investigation.

#### Declaration of Competing Interest

The authors declare that they have no known competing financial interests or personal relationships that could have appeared to influence

Table 4  
Oxygen solubility values (at%) of the elements in the RHEA at 1000 °C [5].

Elements	Nb	Ta	$\alpha$ -Zr	$\beta$ -Zr	$\alpha$ -Hf	$\alpha$ -Ti	$\beta$ -Ti
Oxygen solubility	2.5	3	30	1.5	20	14	1

the work reported in this paper.

## Data Availability

No data was used for the research described in the article.

## References

- [1] B. Gorr, F. Mueller, S. Schellert, H.J. Christ, H. Chen, A. Kauffmann, M. Heilmaier, A new strategy to intrinsically protect refractory metal-based alloys at ultra-high temperatures, *Corros. Sci.* 166 (2020) 108475, <https://doi.org/10.1016/j.corsci.2020.108475>.
- [2] Y. Zhang, T. Fu, J. Zhu, X. Zhang, Microstructure evolution, growth kinetics and formation mechanisms of silicon-rich NbSi<sub>2</sub> coatings on Nb substrate, *J. Mater. Res. Technol.* 24 (2023) 6076–6087, <https://doi.org/10.1016/j.jmrt.2023.04.222>.
- [3] T. Fu, L. Chen, Y. Zhang, F. Shen, J. Zhu, Microstructure and oxidation resistant of Si–NbSi<sub>2</sub> coating on Nb substrate at 800° C and 1000° C, *Ceram. Int.* 49 (13) (2023) 21222–21233, <https://doi.org/10.1016/j.ceramint.2023.03.252>.
- [4] Y. Zhang, T. Fu, L. Yu, K. Cui, J. Wang, F. Shen, K. Zhou, Anti-corrosion coatings for protecting Nb-based alloys exposed to oxidation environments: a review, *Met. Mater. Int.* 29 (1) (2023) 1–17, <https://doi.org/10.1007/s12540-022-01222-8>.
- [5] B. Gorr, S. Schellert, F. Müller, H.J. Christ, A. Kauffmann, M. Heilmaier, Current status of research on the oxidation behavior of refractory high entropy alloys, *Adv. Eng. Mater.* 23 (5) (2021) 2001047. (<https://onlinelibrary.wiley.com/doi/full/10.1002/adem.202001047>).
- [6] O.N. Senkov, G.B. Wilks, D.B. Miracle, C.P. Chuang, P.K. Liaw, Refractory high-entropy alloys, *Intermetallics* 18 (9) (2010) 1758–1765, <https://doi.org/10.1016/j.intermet.2010.05.014>.
- [7] O.N. Senkov, D.B. Miracle, K.J. Chaput, J.P. Couzinie, Development and exploration of refractory high entropy alloys—a review, *J. Mater. Res.* 33 (19) (2018) 3092–3128, <https://doi.org/10.1557/jmr.2018.153>.
- [8] C.S. Kumar, G. Urbikain, P.F. De Lucio, L.N.L. De Lacalle, C. Pérez-Salinas, S. Gangopadhyay, F. Fernandes, Investigating the self-lubricating properties of novel TiSiVN coating during dry turning of Ti6Al4V alloy, *Wear* 532 (2023) 205095, <https://doi.org/10.1016/j.wear.2023.205095>.
- [9] C.S. Kumar, G. Urbikain, L.N.L. De Lacalle, S. Gangopadhyay, F. Fernandes, Investigating the effect of novel self-lubricant TiSiVN films on topography, diffusion and oxidation phenomenon at the chip-tool interface during dry machining of Ti-6Al-4V alloy, *Tribology Int.* 186 (2023) 108604, <https://doi.org/10.1016/j.triboint.2023.108604>.
- [10] F. Shen, L. Yu, T. Fu, Y. Zhang, H. Wang, K. Cui, N. Akhtar, Effect of the Al, Cr and B elements on the mechanical properties and oxidation resistance of Nb–Si based alloys: a review, *Appl. Phys. A* 127 (2021) 1–15, <https://doi.org/10.1007/s00339-021-05013-7>.
- [11] L. Yu, Y. Zhang, T. Fu, J. Wang, K. Cui, F. Shen, Rare earth elements enhanced the oxidation resistance of Mo–Si-based alloys for high temperature application: a review, *Coatings* 11 (9) (2021) 1144, <https://doi.org/10.3390/coatings11091144>.
- [12] C.H. Chang, M. Titus, J.W. Yeh, Oxidation behavior between 700 and 1300° C of refractory TiZrNbHfTa high entropy alloys containing aluminum, *Adv. Eng. Mater.* (2018) 1700948, <https://doi.org/10.1002/adem.201700948>.
- [13] B. Gorr, F. Mueller, H.J. Christ, T. Mueller, H. Chen, A. Kauffmann, M. Heilmaier, High temperature oxidation behavior of an equimolar refractory metal-based alloy 20Nb20Mo20Cr20Ti20Al with and without Si addition, *J. Alloy. Compd.* 688 (2016) 468–477, <https://doi.org/10.1016/j.jallcom.2016.07.219>.
- [14] C.M. Liu, H.M. Wang, S.Q. Zhang, H.B. Tang, A.L. Zhang, Microstructure and oxidation behavior of new refractory high entropy alloys, *J. Alloy. Compd.* 583 (2014) 162–169, <https://doi.org/10.1016/j.jallcom.2013.08.102>.
- [15] Y.K. Cao, L.I.U. Yong, L.I.U. Bin, W.D. Zhang, J.W. Wang, D.U. Meng, Effects of Al and Mo on high temperature oxidation behavior of refractory high entropy alloys, *Trans. Nonferrous Met. Soc. China* 29 (7) (2019) 1476–1483, [https://doi.org/10.1016/S1003-6326\(19\)60504-5](https://doi.org/10.1016/S1003-6326(19)60504-5).
- [16] K.S. Chan, Alloying effects on fracture mechanisms in Nb-based intermetallic in-situ composites, *Mater. Sci. Eng. A* 329–331 (Supplement C) (2002) 513–522, [https://doi.org/10.1016/S0921-5093\(01\)01502-7](https://doi.org/10.1016/S0921-5093(01)01502-7).
- [17] Y. Zhang, T. Fu, L. Yu, F. Shen, J. Wang, K. Cui, Improving oxidation resistance of TZM alloy by deposited Si–MoSi<sub>2</sub> composite coating with high silicon concentration, *Ceram. Int.* 48 (14) (2022) 20895–20904, <https://doi.org/10.1016/j.ceramint.2022.04.080>.
- [18] Y. Zhang, L. Yu, T. Fu, J. Wang, F. Shen, K. Cui, Microstructure evolution and growth mechanism of Si–MoSi<sub>2</sub> composite coatings on TZM (Mo-0.5 Ti-0.1 Zr-0.02 C) alloy, *J. Alloy. Compd.* 894 (2022) 162403, <https://doi.org/10.1016/j.jallcom.2021.162403>.
- [19] K.H.E. Stern, *Metallurgical and Ceramic Protective Coatings*, Springer Netherlands, 1996.
- [20] S. Sheikh, L. Gan, T.K. Tsao, H. Murakami, S. Shafeie, S. Guo, Aluminizing for enhanced oxidation resistance of ductile refractory high-entropy alloys, *Intermetallics* 103 (2018) 40–51, <https://doi.org/10.1016/j.intermet.2018.10.004>.
- [21] G. Yi, Y. Ding, Y. Cheng, P. Zhang, X. Wang, X. Liang, Development and oxidation behavior of high entropy silicide (NbMoTaWV) Si<sub>2</sub> coatings on NbMoTaWV alloy, *J. Alloy. Compd.* 916 (2022) 165384, <https://doi.org/10.1016/j.jallcom.2022.165384>.
- [22] J. Kuang, P. Zhang, Q. Wang, Z. Hu, X. Liang, B. Shen, Formation and oxidation behavior of refractory high-entropy silicide (NbMoTaW) Si<sub>2</sub>coating, *Corros. Sci.* 198 (2022) 110134, <https://doi.org/10.1016/j.corsci.2022.110134>.
- [23] W. Yang, K. Choi, C. Choi, J.S. Park, Degradation properties of refractory MoNbTaVW high-entropy alloys with simultaneous Si/Al pack cementation coatings under high-temperature flame tests, *Oxid. Met.* 96 (5) (2021) 557–569, <https://doi.org/10.1007/s11085-021-10072-5>.
- [24] T.M. Butler, K.J. Chaput, J.R. Dietrich, O.N. Senkov, High temperature oxidation behaviors of equimolar NbTiZrV and NbTiZrCr refractory complex concentrated alloys (RCCAs), *J. Alloy. Compd.* 729 (2017) 1004, <https://doi.org/10.1016/j.jallcom.2017.09.164>.
- [25] J. Zheng, X. Hou, X. Wang, Y. Meng, X. Zheng, L. Zheng, Isothermal oxidation mechanism of a newly developed Nb–Ti–V–Cr–Al–W–Mo–Hf alloy at 800–1200 °C, *Int. J. Refract. Met. Hard Mater.* 54 (2016) 322, <https://doi.org/10.1016/j.ijrmhm.2015.08.012>.
- [26] M. Pole, M. Sadeghilaridjani, J. Shittu, A. Ayyagari, S. Mukherjee, High temperature wear behavior of refractory high entropy alloys based on 4-5-6 elemental palette, *J. Alloy. Compd.* 843 (2020) 156004, <https://doi.org/10.1016/j.jallcom.2020.156004>.
- [27] K. Patel, C. Mahajan, S. Muskeri, S. Mukherjee, Corrosion behavior of refractory high-entropy alloys in LiNaK molten salts, *Metals* 13 (3) (2023) 450, <https://doi.org/10.3390/met13030450>.
- [28] K. Patel, M. Sadeghilaridjani, M. Pole, S. Mukherjee, Hot corrosion behavior of refractory high entropy alloys in molten chloride salt for concentrating solar power systems, *Sol. Energy Mater. Sol. Cells* 230 (2021) 111222, <https://doi.org/10.1016/j.solmat.2021.111222>.
- [29] M. Sadeghilaridjani, A. Ayyagari, S. Muskeri, V. Hasannaeimi, R. Salloom, W. Y. Chen, S. Mukherjee, Ion irradiation response and mechanical behavior of reduced activity high entropy alloy, *J. Nucl. Mater.* 529 (2020) 151955, <https://doi.org/10.1016/j.jnucmat.2019.151955>.
- [30] Ö.S. Böülübaş, T. Serindağ, U. Gürol, A. Günen, G. Çam, Improving oxidation resistance of wire arc additive manufactured Inconel 625 Ni-based superalloy by pack aluminizing, *CIRP J. Manuf. Sci. Technol.* 46 (2023) 89–97, <https://doi.org/10.1016/j.cirpj.2023.07.011>.
- [31] U. Gürol, Y. Altinay, A. Günen, Ö.S. Böülübaş, M. Koçak, G. Çam, Effect of powder-pack aluminizing on microstructure and oxidation resistance of wire arc additively manufactured stainless steels, *Surf. Coat. Technol.* 468 (2023) 129742, <https://doi.org/10.1016/j.surfcoat.2023.129742>.
- [32] M. Sadeghilaridjani, M. Pole, S. Jha, S. Muskeri, N. Ghodki, S. Mukherjee, Deformation and tribological behavior of ductile refractory high-entropy alloys, *Wear* 478–479 (2021) 203916, <https://doi.org/10.1016/j.wear.2021.203916>.
- [33] C.T. Yeh, W.H. Tuan, Oxidation mechanism of aluminum nitride revisited, *J. Adv. Ceram.* 6 (2017) 27–32, <https://doi.org/10.1007/s40145-016-0213-1>.
- [34] L. Henry, J.H. Russell, H.I. Kelly, The system Al<sub>4</sub>C<sub>3</sub>–AlN–Al<sub>2</sub>O<sub>3</sub>: Powder Forming and Sintering Behavior, Phase Identification and Refractory Composition Properties, 7320, U.S. Bureau of Mines, RI, 1969.
- [35] F. Müller, B. Gorr, H.-J. Christ, H. Chen, A. Kauffmann, M. Heilmaier, Effect of microalloying with silicon on high-temperature oxidation resistance of novel refractory high-entropy alloy Ta–Mo–Cr–Ti–Al, *Mater. High. Temp.* 35 (1–3) (2018) 168–176, <https://doi.org/10.1080/09603409.2017.1389115>.
- [36] L. Backman, J. Gild, J. Luo, E.J. Opila, Theoretical predictions of preferential oxidation in refractory high entropy materials, *Acta Mater.* 197 (2020) 20–27, <https://doi.org/10.1016/j.actamat.2020.07.003>.
- [37] The Interactive Ellingham Diagram, DoITPoMS. ([https://www.doitpoms.ac.uk/tlp/1\\_ib/Ellingham\\_diagrams/interactive.php](https://www.doitpoms.ac.uk/tlp/1_ib/Ellingham_diagrams/interactive.php)).
- [38] N. Yurchenko, E. Panina, S. Zhrebts, G. Salishchev, N. Stepanov, Oxidation behavior of refractory AlNbTiVZr0.25 high entropy alloy, *Materials* 11 (12) (2018) 2526, <https://doi.org/10.3390/ma1112256>.
- [39] H. Jiang, M. Hiroishi, Y. Lu, H. Imanari, Effect of Nb on the high temperature oxidation of Ti- (0–50 at%) Al, *Scr. Mater.* 46 (9) (2002) 639–643, [https://doi.org/10.1016/S1359-6462\(02\)00042-8](https://doi.org/10.1016/S1359-6462(02)00042-8).
- [40] M. Yoshihara, K. Miura, Effects of Nb addition on oxidation behavior of TiAl, *Intermetallics* 3 (5) (1995) 357–363, [https://doi.org/10.1016/0966-9795\(95\)94254-C](https://doi.org/10.1016/0966-9795(95)94254-C).
- [41] S. Sheikh, L. Gan, A. Ikeda, H. Murakami, S. Guo, Alloying effect on the oxidation behavior of a ductile Al<sub>0.5</sub>Cr<sub>0.25</sub>Nb<sub>0.5</sub>Ta<sub>0.5</sub>Ti<sub>1.5</sub> refractory high entropy alloy, *Mater. Today Adv.* 7 (2020) 100104, <https://doi.org/10.1016/j.mtadv.2020.100104>.
- [42] R. Ruh, G.H. Hollenberg, E.G. Charles, V.A. Patel, Phase relations and thermal expansion in the system HfO<sub>2</sub>–TiO<sub>2</sub>, *J. Am. Ceram. Soc.* 59 (11–12) (1974) 495–499, <https://doi.org/10.1111/j.1151-2916.1976.tb09416.x>.
- [43] M.C.C. Morales, C.R. Aita, Intrinsic metastability of orthorhombic HfTiO<sub>4</sub> in thin film hafnia-titania, *Appl. Phys. Lett.* 98 (2011) 051909, <https://doi.org/10.1063/1.3551543>.
- [44] J.P. Coutures, J. Coutures, The system HfO<sub>2</sub>–TiO<sub>2</sub>, *J. Am. Ceram. Soc.* 70 (6) (1987) 383–387, <https://doi.org/10.1111/j.1151-2916.1987.tb05655.x>.
- [45] W.H. Tuan, W.B. Chou, Preparation of Al<sub>2</sub>O<sub>3</sub>–AlN–Ni composites. *J. Am. Ceram. Soc.* 80 (9) (1997) 2418–2420.
- [46] T. Yener, K.D. Doleker, A. Erdogan, M. Oge, Y. Er, A.C. Karaoglanli, A. C. S. Zeytin, Wear and oxidation performances of low temperature aluminized IN600, *Surf. Coat. Technol.* 436 (2022) 128295, <https://doi.org/10.1016/j.surfcoat.2022.128295>.
- [47] K.M. Döleker, A. Erdogan, T. Yener, A.C. Karaoglanli, O. Uzun, M.S. Gök, S. Zeytin, Enhancing the wear and oxidation behaviors of the Inconel 718 by low temperature aluminizing, *Surf. Coat. Technol.* 412 (2021) 127069, <https://doi.org/10.1016/j.surfcoat.2021.127069>.

- [48] A.S. Ulrich, M.C. Galetz, M. C, Protective aluminide coatings for refractory metals, *Oxid. Met.* 86 (5-6) (2016) 511–535, <https://doi.org/10.1007/s11085-016-9650-z>.
- [49] J. Jayaraj, P. Thirathipiwat, J. Han, A. Gebert, Microstructure, mechanical and thermal oxidation behavior of AlNbTiZr high entropy alloy, *Intermetallics* 100 (2021) 9–19, <https://doi.org/10.1016/j.intermet.2018.05.015>.
- [50] S. Sheikh, M.K. Bijaksana, A. Motallebzadeh, S. Shafeie, A. Lozinko, L. Gan, T. K. Tsao, U. Klement, D. Canadinc, H. Murakami, S. Guo, Accelerated oxidation in ductile refractory high entropy alloys, *Intermetallics* 97 (2018) 58–66, <https://doi.org/10.1016/j.intermet.2018.04.001>.